



**HAL**  
open science

## The Pristine survey XI: the FORS2 sample

E. Caffau, P. Bonifacio, L. Sbordone, A. D. M. Matas Pinto, P. François, P. Jablonka, C. Lardo, Nicolas F. Martin, E Starkenburg, D Aguado, et al.

► **To cite this version:**

E. Caffau, P. Bonifacio, L. Sbordone, A. D. M. Matas Pinto, P. François, et al.. The Pristine survey XI: the FORS2 sample. Monthly Notices of the Royal Astronomical Society, 2020, 493 (4), pp.4677-4691. 10.1093/mnras/staa589 . obspm-02508664

**HAL Id: obspm-02508664**

**<https://hal-obspm.ccsd.cnrs.fr/obspm-02508664v1>**

Submitted on 15 Mar 2020

**HAL** is a multi-disciplinary open access archive for the deposit and dissemination of scientific research documents, whether they are published or not. The documents may come from teaching and research institutions in France or abroad, or from public or private research centers.

L'archive ouverte pluridisciplinaire **HAL**, est destinée au dépôt et à la diffusion de documents scientifiques de niveau recherche, publiés ou non, émanant des établissements d'enseignement et de recherche français ou étrangers, des laboratoires publics ou privés.

# The *Pristine* survey XI: the FORS2 sample

E. Caffau,<sup>1\*</sup> P. Bonifacio,<sup>1</sup> L. Sbordone,<sup>2</sup> A. M. Matas Pinto,<sup>1</sup> P. François,<sup>3</sup>  
 P. Jablonka,<sup>4,1</sup> C. Lardo,<sup>4</sup> N. F. Martin,<sup>5,6</sup> E. Starkenburg,<sup>7</sup> D. Aguado,<sup>8</sup>  
 J. I. González-Hernández,<sup>9,10</sup> K. Venn,<sup>11</sup> L. Mashonkina,<sup>12</sup> and F. Sestito<sup>5</sup>

<sup>1</sup>GEPI, Observatoire de Paris, Université PSL, CNRS, Place Jules Janssen, 92190 Meudon, France

<sup>2</sup>European Southern Observatory, Alonso de Cordova 3107, Vitacura, Casilla 19001, Santiago, Chile

<sup>3</sup>GEPI, Observatoire de Paris, Université PSL, CNRS, 77 Av. Denfert-Rochereau, 75014 Paris, France

<sup>4</sup>Institute of Physics, Laboratoire d'Astrophysique, Ecole Polytechnique Fédérale de Lausanne (EPFL), Observatoire de Sauverny, CH-1290 Versoix, Switzerland

<sup>5</sup>Université de Strasbourg, CNRS, Observatoire astronomique de Strasbourg, UMR 7550, F-67000, France

<sup>6</sup>Max-Planck-Institut für Astronomie, Königstuhl 17, D-69117, Heidelberg, Germany

<sup>7</sup>Leibniz Institute for Astrophysics Potsdam (AIP), An der Sternwarte 16, D-14482 Potsdam, Germany

<sup>8</sup>Institute of Astronomy, University of Cambridge, Madingley Road, Cambridge CB3 0HA, UK

<sup>9</sup>Instituto de Astrofísica de Canarias, Vía Láctea, 38205 La Laguna, Tenerife, Spain

<sup>10</sup>Departamento de Astrofísica, Universidad de La Laguna, E-38206 La Laguna, Tenerife, Spain

<sup>11</sup>Department of Physics and Astronomy, University of Victoria, Victoria, BC V8W 3P2, Canada

<sup>12</sup>Institute of Astronomy, Russian Academy of Sciences, RU-119017 Moscow, Russia

Accepted XXX. Received YYY; in original form ZZZ

## ABSTRACT

Extremely metal-poor (EMP) stars are old objects that mostly formed very early after the Big Bang. They are rare and, to select them, we have to rely on low-resolution spectroscopic or photometric surveys; specifically the combination of narrow- and broad-band photometry provides a powerful and time efficient way to select metal-poor stars. The *Pristine* photometric Survey is using the CFHT MegaCam wide field imager to obtain narrow-band photometry by utilising a filter centred at 395.2 nm on the CaII-H and -K lines. Gaia DR 2 is providing us the wide band photometry as well as parallaxes. Follow-up observations of metal-poor candidates allowed us to improve our photometric calibrations. In this paper of the series we analyse metal-poor stars observed with FORS2 at VLT. We demonstrate the *Pristine* calibration adopted in this work to be able to provide metallicities accurate to  $\pm 0.3$  dex for metal-poor giant stars with good parallaxes, while it performs poorly for dwarf and turn off stars, whatever the accuracy on the parallaxes. We find some metal-poor and very metal-poor stars that are not enhanced in  $\alpha$  elements. Such stars have already been found in several other searches, and a higher resolution follow-up of our sample would be useful to put our findings on a firmer ground. This sample of stars analysed has a low fraction of Carbon Enhanced Metal Poor (CEMP) stars, regardless of the definition adopted. This deficiency could indicate a small sensitivity of the *Pristine* filter to carbon abundance, issue to be addressed in the future.

**Key words:** stars: abundances – stars: Population II – Galaxy: abundances – Galaxy: evolution

## 1 INTRODUCTION

The early Universe (about 12.5 Gyr ago or more, corresponding to a redshift  $z > 5$ ) was poor in elements heavier than Helium (Pallottini et al. 2014), since in such limited time only few generations of massive stars could enrich the medium with their nucleosynthetic products. The low-mass (less than  $1 M_{\odot}$ ) stars that formed at that time thus tended to be very

metal-poor (VMP,  $[\text{Fe}/\text{H}] \leq -2$ ) or extremely metal-poor (EMP,  $[\text{Fe}/\text{H}] \leq -3$ ). Thanks to their long life-time, such objects are still observable today, with a photospheric chemical content which is the one of the gas cloud from which they formed. These pristine stars are thus extremely valuable probes into the early stages of the Milky Way evolution (Freeman, & Bland-Hawthorn 2002; Karlsson et al. 2013).

It was long believed that these stars tended to occupy pressure-supported orbits in the MW spheroidal components (Halo and Bulge), with the Outer Halo preferentially

\* E-mail: Elisabetta.Caffau@obspm.fr

constituted by objects accreted from tidally-destroyed dwarf galaxies (White, & Springel 2000; Brook et al. 2007; Gao et al. 2010; Salvadori et al. 2010; Tumlinson 2010; Ishiyama et al. 2016; Starkenburg et al. 2017b; El-Badry et al. 2018; Griffen et al. 2018). However, recent studies exploiting the exquisite astrometric solutions from Gaia Data Release 2 (DR2) (Gaia Collaboration et al. 2018) showed how a significant fraction of EMP stars does in fact inhabit the Milky Way plane (Sestito et al. 2019a,b; Di Matteo et al. 2019) rising questions on the formation of the Milky Way disc, and on the Galaxy in general.

The EMP stars are very rare objects and large amounts of observing time are required to find them. To this end, several projects were devised to observe a relatively large sample of stars via low resolution spectroscopy, followed up by high resolution observation of the most promising candidates (see e.g. Beers et al. 1985, 1992; Christlieb et al. 2008; Caffau et al. 2013b). Anthony-Twarog et al. (2000, and references therein) used a narrow band filter centred on the Ca II HK lines, combined with Strömgren filters, to determine the metallicity of metal poor stars. This approach was effective, however it relied on a pre-selection of candidates (in that case from objective prism spectra) and the photometry had to be acquired one star at the time. The situation changed drastically when narrow band filters of large size that could be coupled with wide field imagers, became available. The first instrument that could perform such a survey was the SkyMapper Telescope that started the still ongoing SkyMapper Southern Sky Survey (Keller et al. 2007; Wolf et al. 2018). With a field of view of 5.7 square degrees, this survey plans to cover all of the southern sky in five wide bands and one narrow band centred on the Ca II HK lines. In this case the metallicities can be determined for all stars in the field and metal-poor stars can be selected for follow-up spectroscopy. Among the highlight results of the SkyMapper Southern Sky Survey, we may cite the discovery of SMSS J031300.36-670839.3 (Keller et al. 2014), currently the star with the lowest upper limit on its iron abundance; the discovery of the most metal-poor stars yet found in the Galactic Bulge (Howes et al. 2015); and the discovery of SMSS J160540.18-144323.1 (Nordlander et al. 2019a), currently the star with the lowest measured iron abundance. Recently (Da Costa et al. 2019a) have presented the results of the low resolution follow-up of the SkyMapper Southern Sky Survey for a sample of stars that is over an order of magnitude larger than the much smaller sample presented here.

Photometric observations, are much less time consuming than single object spectroscopy: more stars are observed at the same time, and fainter objects can be observed with the same telescope size and integration time. However, MP and EMP stars show in their spectra only a relatively small number of metallic lines. This causes all broad-band photometric metallicity indicators to saturate at low metallicity, becoming unusable. Photometric observations that aim at detecting EMP stars need thus to resort to narrow-band photometry centred around strong metallic features. In the low-resolution regime (resolving power on the order of 2000), in the spectrum of a metal-poor star even the (usually very strong) lines of the Mg I b triplet or the infra-red Ca II triplet can become barely detectable. The 392 nm Ca II-K line, on the other hand, remains usually visible in the low-resolution spectrum of EMP stars. This strong indicator of the Ca con-

tent of a star can thus be used as a metallicity indicator when narrow-band photometry centred at about 395.2 nm is used, and metal-poor candidates can be successfully selected this way.

In the Pristine project (Starkenburg et al. 2017a), we use a narrow band filter centred on the Ca II-H and -K lines (*CaHK*), in conjunction with wide band photometry, as a means to obtain metallicity estimates. The *CaHK* photometry is taken with the wide-field imager MegaCam mounted on the Canada France Hawaii Telescope (CFHT). Previously the wide band photometry was taken from the Sloan Digital Sky Survey (SDSS; York et al. 2000) as in (Youakim et al. 2017). The selection was already extremely good with a success rate of about 22% for stars with  $[\text{Fe}/\text{H}] < -3$  (see Youakim et al. 2017). In Bonifacio et al. (2019) we have derived a new calibration where the *CaHK* photometry is combined with Gaia photometry from DR2 and we also take advantage of the parallaxes to deduce the surface gravity, and therefore the evolutionary status of each star. For short we shall refer to this calibration as PristineV in the following since it was introduced in Bonifacio et al. (2019), the fifth paper of the series. Very recently, Aguado et al. (2019a) analysed about 1000 low-resolution spectra of stars selected with the Pristine photometry, and could confirm the high success of this search for metal-poor stars based on photometry

From a sample of 115 Pristine candidates observed at high-resolution, Venn et al. (2020) derived detailed chemical abundances for 28 newly discovered metal-poor stars. The discovery of Pristine\_221.8781+9.7844, the second star known to have  $[\text{Fe}/\text{H}] < -4.5$  and with no evidence of enhancement in carbon (Starkenburg et al. 2018), further demonstrates the efficiency of Pristine in selecting EMP candidates.

In this paper we describe the analysis of a sample of metal-poor candidates observed with FORS2 (Appenzeller et al. 1998) at the ESO VLT Antu 8.2 m telescope. Analysing the FORS2 spectra, we were able to derive a metallicity for 135 stars and, for the less metal-poor stars, with the better quality spectra (high signal-to-noise ratio, S/N), we could also derive detailed abundances (C, Mg, Ca, Ti, Ni, Sr and Ba). For the stars with detailed chemical composition, the S/N per pixel at 500 nm was always higher than 60, and in the majority of the cases higher than 80.

## 2 THE FORS2 SAMPLE

### 2.1 Target selection

The purpose of these observations was to verify, and possibly improve, the photometric calibration in the very metal poor regime. For the observations in ESO periods 100 and 101 we used the catalogue of Pristine photometry, as available up to March 2017. The *CaHK* photometry was combined with SDSS *gri* photometry, as described in Starkenburg et al. (2017a); Youakim et al. (2017), to estimate effective temperatures and metallicities. We selected stars with  $g \lesssim 17$  and estimated photometric metallicity  $\leq -2.5$ , no condition was set on the temperature of the stars.

In ESO period 103 the PristineV calibration became available and we used it to select brighter stars with photometric metallicity  $\leq -2.5$ . In this period we observed 57

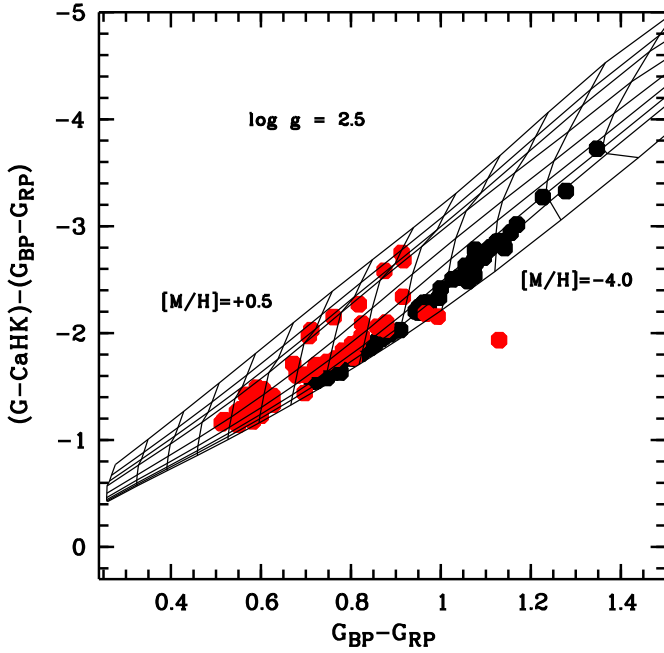


**Figure 1.** Location of the observed stars in the PristineV colour-colour diagram. The stars observed in ESO periods 100 and 101 are shown as red dots, those observed in ESO period 103 as black dots. To guide the eye we superimposed the grid of synthetic colours with  $\log g = 2.5$  and  $-4.0 \leq [M/H] \leq +0.5$ .

stars in the magnitude range  $12 < G < 15$  and  $17$  with  $15 \leq G \leq 17$ . The sample in ESO period 103 is also somewhat biased in favour of cool giants, where we expected the PristineV calibration to work better.

The sample has thus not been selected with a clean and well defined selection function. The location of the selected stars in the PristineV colour-colour diagram is shown in Fig. 1. The colours have been dereddened, as described in Starkenburg et al. (2017a), using the maps described in Schlafly, & Finkbeiner (2011)<sup>1</sup>.

## 2.2 Observations

The observations were acquired in service mode at the ESO Antu 8.2m telescope with the FORS2 instrument. We took long-slit spectra using GRISM 600B+22 with a  $0''.28$  wide slit that provides a resolving power  $R \sim 2800$ . The spectral range covered is 330 nm to 621 nm. We used a  $1 \times 1$  binning of the CCD, corresponding to 0.075 nm/pixel, to avoid undersampling in the blue spectral range. Exposure time was 2762s for each star. For one star, Pristine\_254.5655+13.1590, the observation was repeated twice since the first spectrum was deemed of insufficient quality. Both spectra were subsequently used by coadding them. The program was designed as an “all-weather” one, allowing to

<sup>1</sup> For the Gaia colours we used  $A(G)/A(V) = 0.85926$ ,  $A(G_{BP})/A(V) = 1.06794$ ,  $A(G_{RP})/A(V) = 0.65199$ , with  $A(V)/E(B-V) = 3.1$ . These are the values suggested by the PARSEC isochrones site <http://stev.oapd.inaf.it/cgi-bin/cmd>, (Bressan et al. 2012)

exploit also unfavourable observational conditions. Unsurprisingly most observations were executed in bright time, with poor seeing and transparency conditions. In spite of this, most of the spectra are of good quality, thanks to the large light collecting power of VLT.

The spectra were acquired in three ESO programmes: 0100.D-0559, 0101.D-0227 and 0103.D-0128. In programme 0100.D-0559, 23 out of 48 OBs were executed and 19 spectra were analysed; in programme 0101.D-0227, 43 out of 60 OBs were executed and 41 spectra were analysed; during programme 0103.D-0128, 75 OBs were executed and the 75 spectra (a spectrum for each OB) of 74 stars analysed.

A total of 135 spectra were analysed. Seven were discarded due to poor quality, 30 were used to determine metallicity only, and 98 were used for a full chemical analysis where abundances were determined for several elements.

## 3 ANALYSIS

### 3.1 Radial Velocities

The radial velocities were derived by template-matching (see e.g. Koposov et al. 2011, and references therein). As template for each star we used a synthetic spectrum computed with the parameters derived (see section 3.3). Before performing the match the spectrum was normalised using as continuum estimate a maximum filter with a 25 pixels kernel. The procedure was iterative, a first guess of the radial velocity was derived using the photometric estimate of the metallicity. This allowed to shift the spectrum to zero radial velocity to perform the chemical analysis. The final radial velocity, reported in Table 3, was derived using a template with the spectroscopic metallicity. In Table 3, we report the statistical error on the radial velocity,  $\delta V_{st}$ , that reflects the signal-to-noise ratio of the spectrum and is estimated from the  $\chi^2$  of the spectrum-template match. On average, at similar metallicity, the cooler stars have a lower statistical uncertainty because their spectra contain more lines than the warmer stars.

FORS2 is mounted at the Cassegrain focus and suffers from flexures that depend on the zenith distance, as documented in the FORS2 user manual<sup>2</sup>. In Table 3, we report the maximum radial velocity shift,  $\delta V_{sy}$ , for the zenith angle at which the star was observed. This is similar to what we did in Caffau et al. (2018), where we used a different grism.

Another source of systematic error in our radial velocities is the change in temperature and pressure between the time in which each spectrum was taken and the time at which the calibration arc was taken (usually in the day following the observation).

Finally one should keep in mind that with the grism we are using, decentering the target on the slit by  $0''.1$  implies a shift of about  $38 \text{ km s}^{-1}$  in radial velocity. We have no telluric absorption lines in our spectra, so there is no hope of correcting for this effect. We are observing with a slit that is at least a factor of three narrower than the seeing during the observations, for a long exposure. We may therefore hope that both the seeing and errors in tracking contribute

<sup>2</sup> [http://www.eso.org/sci/facilities/paranal/instruments/fors/doc/VLT-MAN-ESO-13100-1543\\_P03.pdf](http://www.eso.org/sci/facilities/paranal/instruments/fors/doc/VLT-MAN-ESO-13100-1543_P03.pdf)

to a uniform illumination of the slit. This would make the decentering errors small.

In order to have an external comparison on our radial velocities we searched in SIMBAD<sup>3</sup> for matches with our stars, we found nine matches, of which four have published radial velocities. The data available for these four stars is summarised in Table 1. If we compare our measured radial velocities with the published radial velocities we find a mean offset of  $17 \text{ km s}^{-1}$  and a standard deviation of  $15 \text{ km s}^{-1}$ . In principle the offsets both for flexures and difference in temperature and pressure should be corrected by using the sky emission lines in the spectra. In our spectra the most prominent sky emission line is [O I] 557 nm. We measured the position of eight unblended emission lines on the sky spectrum of each of the four stars in Table 1 and cross-correlated the measured positions with the catalogue of sky emission lines of Hamuschik (2003). In this way we determined a shift to be applied to each measured radial velocity, ranging from  $-25 \text{ km s}^{-1}$  to  $+20 \text{ km s}^{-1}$ . After applying this correction the comparison with the external radial velocities becomes worse, the offset is still around  $17 \text{ km s}^{-1}$ , but the standard deviation rises to  $33 \text{ km s}^{-1}$ . The comparison is based on a limited size sample, however there is a clear indication that applying the correction derived from sky emission lines does not improve the accuracy of the radial velocities.

### 3.2 Orbital parameters

We infer the orbital parameters for the stars with  $[\text{Fe}/\text{H}] \leq -2.5$  in order to verify if such low-metallicity stars can inhabit the thick disc region as discovered by Sestito et al. (2019a); Di Matteo et al. (2019); Sestito et al. (2019b). We follow the Bayesian inference methods described in Sestito et al. (2019a) in order to calculate the distances and the orbital parameters of our sample. For the calculation of the orbits we use Galpy package (Bovy 2015), and we choose the *MWPotential14* as the MW gravitational potential enhancing the mass of the halo, with a mass of  $1.2 \cdot 10^{12} M_{\odot}$  compatible with the value from Bland-Hawthorn, & Gerhard (2016) (vs.  $0.8 \cdot 10^{12} M_{\odot}$  for the halo used in *MWPotential14*). We assume 8.0 kpc as the distance between the Sun and the Galactic centre, that the Local Standard of Rest circular velocity is  $V_c = 239 \text{ km s}^{-1}$ , and that the peculiar motion of the Sun is:  $U_0 = 11.10 \text{ km s}^{-1}$ ,  $V_0 + V_c = 251.24 \text{ km s}^{-1}$ ,  $W_0 = 7.25 \text{ km s}^{-1}$ , as described in Schönrich et al. (2010). The kinematics of the stars are discussed in Section 4.1.

### 3.3 Stellar parameters and chemical abundances

We used the Gaia parallax, combined with the Gaia G photometry, to derive the surface gravity, due to the fact that the stars are relatively bright, so they have generally accurate parallaxes. We then used the PristineV calibration to derive effective temperature and metallicity. Four of the stars have negative parallaxes, Pristine\_180.1247+03.4435, Pristine\_228.1376+12.2612, Pristine\_233.5160+15.9466 and Pristine\_247.2527+05.6626. For these stars we adopted the

distances derived by Bailer-Jones et al. (2018), that are derived using a Bayesian approach using an exponentially decreasing star density. The uncertainty on the effective temperature we derive is of 125 K for all stars. It is due to the  $T_{\text{eff}}$  step in the grid used, which is of 250 K. For the gravity, the uncertainty is related to the uncertainty on the parallax. For the stars for which we derive detailed abundances, the uncertainty on  $\log g$  is within 0.5 dex, except for four stars (Pristine\_149.5692+15.4688, Pristine\_186.6431+02.5876, Pristine\_209.5181+09.3536, Pristine\_251.2069+14.7890) for which the uncertainty was up to 1 dex. Obviously, for the stars for which the uncertainty in the parallax is larger than the parallax itself, there is no lower limit in the gravity.

With these values of effective temperature and gravity, to derive the abundances or the metallicity, the secured spectra have been analysed with MyGIsFOS (Sbordone et al. 2014), an automatic pipeline that compares the profile of each selected feature to a grid of pre-computed synthetic spectra. The grid we used have been computed with SYNTHÉ (see Kurucz 2005; Sbordone et al. 2004) and based on grids of ATLAS 12 models (Kurucz 2005). Due to the wide parameter space, we have four grids for metal-poor dwarf, sub-giant and giant stars and for metal-rich dwarf stars. Their characteristics are:

- Metal-poor giants

$T_{\text{eff}}$  range from 4000 to 5200 K, step 200 K;  
 $\log g$  range form 0.5 to 3.0, step 0.5;  
 microturbulence: from 1 to 3 km/s, step 1 km/s;  
 $\alpha$ -enhancement: from  $-0.4$  to  $+0.4$ , step 0.4;  
 metallicity: from  $-4.0$  to  $-1.0$ , step 0.5.

- Metal-poor sub-giants

$T_{\text{eff}}$  range from 5200 to 5600 K, step 200 K;  
 $\log g$  range form 2.0 to 3.5, step 0.5;  
 microturbulence: from 1 to 3 km/s, step 1 km/s;  
 $\alpha$ -enhancement: from  $-0.4$  to  $+0.4$ , step 0.4;  
 metallicity: from  $-3.5$  to  $-1.0$ , step 0.5.

- Metal-poor dwarfs

$T_{\text{eff}}$  range from 5600 to 6400 K, step 200 K;  
 $\log g$  range form 3.0 to 4.5, step 0.5;  
 microturbulence: from 0 to 2 km/s, step 1 km/s;  
 $\alpha$ -enhancement: from  $-0.4$  to  $+0.4$ , step 0.4;  
 metallicity: from  $-4.0$  to  $-1.0$ , step 0.5.

- Metal-rich dwarfs

$T_{\text{eff}}$  range from 5600 to 6400 K, step 200 K;  
 $\log g$  range form 3.0 to 4.5, step 0.5;  
 microturbulence: from 0 to 2 km/s, step 1 km/s;  
 $\alpha$ -enhancement: from  $-0.4$  to  $+0.4$ , step 0.4;  
 metallicity: from  $-1.0$  to  $+0.5$ , step 0.5.

As solar abundances we used the values listed in Table 2, because these values reproduce well the sound speed in the Sun as determined by helioseismic observations (Antia, & Basu 2011).

For the chemical analysis of each star, effective temperature and surface gravity are kept fixed and the abundance from each feature (line or, in the case of low resolution, also blends of lines) is derived by  $\chi^2$  minimisation.

<sup>3</sup> <http://simbad.u-strasbg.fr/simbad/>



**Table 1.** Literature data for our targets.

star	SIMBAD ID	$V_{\text{rad}}$ kms $^{-1}$ our	$V_{\text{rad}}$ kms $^{-1}$ literature	$\delta V_{\text{rad}}$ kms $^{-1}$	Ref. $V_{\text{rad}}$	$T_{\text{eff}}$ K	$\log g$ cgs	[Fe/H] dex	Ref. atm. par.
Pristine_218.1282+09.1135	SDSS J143230.77+090648.5	-215	-235	2	SDSS DR15 (A)	5456	2.80	-2.62	(T)
Pristine_242.4476+16.9021	SDSS J160947.42+165407.4	+62	+26	2	SDSS DR15 (A)	5298	2.49	-2.56	(T)
Pristine_254.4746+11.3806	TYC 983-1782-1	-250	-230.52	1.16	Gaia DR2 (G)	4932			(G)
Pristine_151.6456+15.9545	SDSS J100634.93+155716.1	+82	70.3	2.2	(S)				

(A): Aguado et al. (2019b); (G): Gaia Collaboration et al. (2018); (S): Simon et al. (2011); (T): Tan et al. (2014)

**Table 2.** Solar abundances.

Element	A(X)	Reference
C	8.50	Caffau et al. (2010)
N	7.86	Caffau et al. (2010)
Mg	7.54	Lodders et al. (2009)
Ca	6.33	Lodders et al. (2009)
Ti	4.90	Lodders et al. (2009)
Cr	5.64	Lodders et al. (2009)
Fe	7.52	Caffau et al. (2010)
Ni	6.23	Lodders et al. (2009)
Sr	2.92	Lodders et al. (2009)
Ba	2.17	Lodders et al. (2009)

The micro-turbulence ( $v_t$ ) cannot be derived from the low-resolution spectra. For the evolved stars, we assumed always  $v_t \geq 1.5$  km/s, and we divided following the gravity: for  $\log g \leq 2$  we assumed  $v_t = 2.0$  km/s; for  $2 < \log g < 3$  we assumed  $v_t = 1.8$  km/s; for  $3 \leq \log g \leq 4$  we assumed  $v_t = 1.5$  km/s. For unevolved stars ( $\log g \geq 4$ ) we assumed two micro-turbulence values according to the effective temperature as: for  $T_{\text{eff}} \leq 6000$  K we assumed  $v_t = 1.0$  km/s as for the Sun and for  $T_{\text{eff}} > 6000$  K we assumed  $v_t = 1.5$  km/s as for Procyon.

In Figure 2, the analysed stars are shown, compared to PARSEC isochrones (Bressan et al. 2012). From the figure one can see that in the ESO period 103 we changed strategy and selected mainly stars in the red giant branch. These stars are more sensitive to the PristineV calibration we used in the selection and as a consequence ESO period 103 observations have been generally more successful than the previous two, suggesting that the use of parallaxes and the choice of cooler stars have improved the selection efficiency. In the figure, we divided the stars in metal-poor (black symbols) and metal-rich (red symbols) by using the Ca abundance, because we could derive it from a larger sample of stars, by analysing the Ca II-K line. Few stars appear in the figure displaced with respect to the isochrones. We are not worried about it, for two main reasons. (1) From our previous investigations (Bonifacio et al. 2019), we analysed stars that are metal-poor but lie on isochrones of young ages, this could simple be due to the fact that they are evolved blue stragglers and that the parameters derived by the PristineV calibration are perfectly consistent with the isochrone of the appropriate age; (2) also if in fact these stars have a non-accurate distance and as a consequence they have in fact a larger surface gravity, this is not a problem for the chemical investigation: a change of 0.5 dex in the surface gravity changes the abundances of the elements by about 0.1 dex

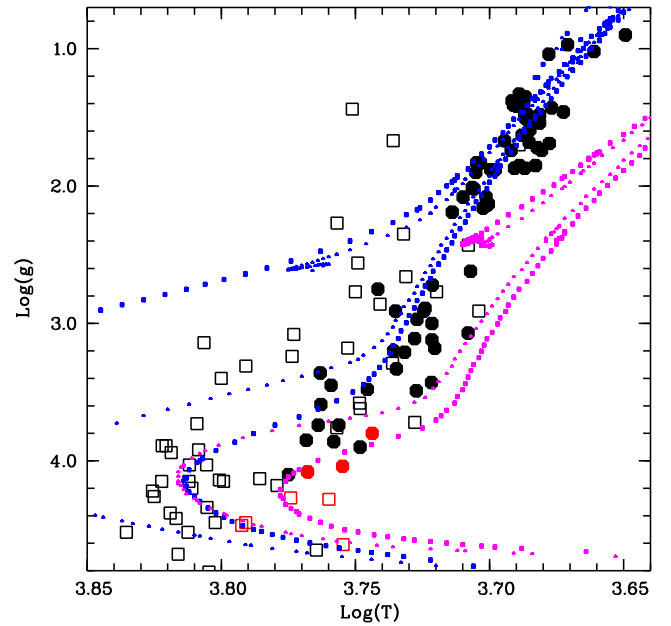


**Figure 2.** Stellar parameters of the observed stars in a  $T_{\text{eff}} - \log g$  diagram, compared to isochrones (Bressan et al. 2012) (ages of 5 and 12.6 Gyr, in blue metallicity of  $-2.0$  and in violet metallicity of  $-0.5$ ). Filled symbols corresponds to stars observed in ESO period 103, empty symbols stars observed in ESO periods 100 and 101. Red symbols are stars with  $A(\text{Ca}) \geq 5.9$  and black symbols  $A(\text{Ca}) < 5.9$ .

or less for the neutral elements, which is much smaller than the uncertainties we derive and expect. Anyway, for the subsample of stars for which we have an abundance derived from two stages of ionisation of Ti and Fe, the comparison on the abundances we derive indicates that the surface gravity we derive is absolutely reasonable.

In Table 3 the stellar parameters are reported: the stars are ordered in groups by right ascension and the groups are organised as follows: the first group contains the 98 stars for which detailed chemical investigation was done; the following 20 stars have a metallicity derived from the spectrum and a Ca abundance from the Ca II-K line; the next ten stars have only the Ca abundance from the Ca II-K line; for the latest seven stars we could not derive any abundance. To give an idea on the quality of the observations, two spectra are shown in Figure 3.

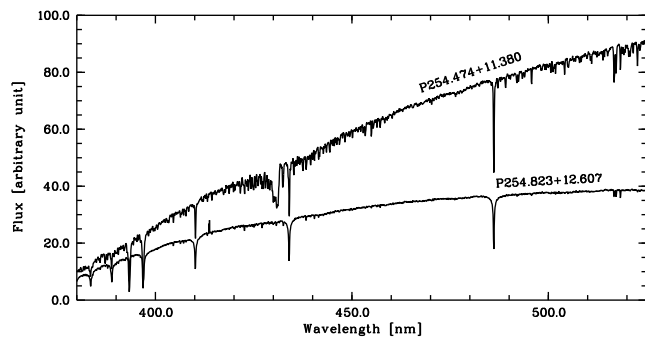


**Figure 3.** Two observed spectra: Pristine.254.4746+11.3806 (4818/1.85/−3.08) and Pristine.254.8233+12.6074 (5793/3.59/−3.12). Both spectra have S/N per pixel at 500 nm of about 100.





Star	RA J2000	Dec J2000	$T_{\text{eff}}$ K	$\log g$ cgs	$\xi$ $\text{kms}^{-1}$	[Fe/H] <sub>phot</sub> dex	[Fe/H] dex	[Ca/H] <sub>CaK</sub> dex	$V_{\text{rad}}$	$\delta V_{\text{st}}$ $\text{kms}^{-1}$	$\delta$
Pristine_241.4951+12.2706	16:05:58.83	12:16:14.5	5604	3.58 ± 0.26	1.50	-1.68	-2.55 ± 0.27	-2.07 ± 0.20	-16	5	
Pristine_241.5968+04.5933	16:06:23.23	04:35:35.9	4910	1.41 ± 0.26	2.00	-2.38	-2.24 ± 0.19	-1.93 ± 0.20	-193	4	
Pristine_241.9145+09.8595	16:07:39.48	09:51:34.4	4687	0.97 ± 0.27	2.00	-2.43	-2.20 ± 0.22	-1.94 ± 0.20	+65	3	
Pristine_242.0410+15.8022	16:08:09.84	15:48:07.8	4874	1.63 ± 0.22	2.00	-2.59	-3.07 ± 0.19	-2.66 ± 0.20	-278	5	
Pristine_242.1683+11.6600	16:08:40.39	11:39:35.9	4841	1.59 ± 0.28	2.00	-2.41	-2.42 ± 0.18	-2.11 ± 0.20	-160	4	
Pristine_242.4016+05.8580	16:09:36.38	05:51:28.8	5264	2.72 ± 0.12	1.80	-2.76	-2.83 ± 0.18	-2.37 ± 0.20	-136	5	
Pristine_242.4481+17.4384	16:09:47.54	17:26:18.1	4895	1.42 ± 0.21	2.00	-2.33	-2.36 ± 0.19	-2.15 ± 0.20	-112	4	
Pristine_242.4476+16.9021	16:09:47.42	16:54:07.3	5017	2.13 ± 0.30	1.80	-2.33	-2.81 ± 0.20	-2.40 ± 0.20	+62	5	
Pristine_242.9404+11.7356	16:11:45.69	11:44:08.0	4460	0.90 ± 0.23	2.00	-2.34	-2.39 ± 0.20	-2.14 ± 0.20	-52	3	
Pristine_243.2008+06.8892	16:12:48.18	06:53:21.2	5683	4.61 ± 0.09	1.00	+0.50	-0.06 ± 0.35	0.05 ± 0.20	+18	2	
Pristine_243.5457+12.5189	16:14:10.98	12:31:07.9	6179	4.45 ± 0.16	1.50	+0.43	-0.37 ± 0.30	-0.28 ± 0.20	+34	3	
Pristine_243.8922+04.8666	16:15:34.12	04:51:59.8	5601	3.90 ± 0.02	1.50	-2.65	-0.99 ± 0.16	-0.95 ± 0.20	-20	3	
Pristine_244.7163+09.2647	16:18:51.91	09:15:52.9	5325	4.39 ± 0.32	1.00		-0.71 ± 0.23		-5	3	
Pristine_245.0350+07.0160	16:20:08.40	07:00:57.7	4858	1.51 ± 0.18	2.00	-2.33	-2.65 ± 0.29	-2.35 ± 0.20	-12	4	
Pristine_245.9038+05.9390	16:23:36.94	05:56:20.6	6390	4.03 ± 0.24	1.50	-0.74	-1.17 ± 0.35	-1.05 ± 0.20	-82	4	
Pristine_246.0821+09.9611	16:24:19.70	09:57:39.8	5956	4.10 ± 0.24	1.00	-2.47	-2.32 ± 0.30	-2.26 ± 0.20	-33	5	
Pristine_247.3535+10.1964	16:29:24.84	10:11:46.8	5175	2.19 ± 0.27	1.80	-2.54	-2.79 ± 0.34	-2.76 ± 0.20	+45	5	
Pristine_247.3761+16.8149	16:29:30.25	16:48:53.7	5516	2.75 ± 0.10	1.80	-2.48	-3.43 ± 0.35	-2.83 ± 0.20	-299	6	
Pristine_247.6492+09.8880	16:30:35.81	09:53:16.8	4861	1.35 ± 0.20	2.00	-2.96	-2.67 ± 0.20	-2.42 ± 0.20	+119	4	
Pristine_248.3014+09.7034	16:33:12.31	09:42:12.3	6684	4.26 ± 0.18	1.50	-0.99	-2.07 ± 0.52	-1.54 ± 0.20	-29	5	
Pristine_248.8084+17.4032	16:35:14.01	17:24:11.6	4863	1.48 ± 0.13	2.00	-2.59	-1.76 ± 0.19	-1.74 ± 0.20	-64	4	
Pristine_249.1867+05.9980	16:36:44.81	05:59:52.8	6178	3.31 ± 0.36	1.50	-1.19	-2.09 ± 0.44	-1.48 ± 0.20	-67	10	
Pristine_249.6131+05.3269	16:38:27.17	05:19:37.6	5303	2.91 ± 0.15	1.80	-2.64	-1.98 ± 0.17	-1.69 ± 0.20	-257	4	
Pristine_250.2762+09.2517	16:41:06.30	09:15:06.1	5704	3.74 ± 0.26	1.50	-2.47	-2.63 ± 0.26	-2.56 ± 0.20	+70	5	
Pristine_251.2012+16.7235	16:44:48.28	16:43:24.7	4801	1.48 ± 0.29	2.00	-2.42	-2.61 ± 0.20	-2.22 ± 0.20	-366	4	
Pristine_251.2069+14.7890	16:44:49.67	14:47:20.4	5612	2.56 ± 0.74	1.80	-1.23	-1.90 ± 0.30	-1.26 ± 0.20	-252	5	
Pristine_252.3631+13.2237	16:49:27.13	13:13:25.3	4886	1.33 ± 0.24	2.00	-2.59	-2.67 ± 0.27	-2.40 ± 0.20	-18	4	
Pristine_252.4992+05.4959	16:49:59.81	05:29:45.0	4851	1.48 ± 0.15	2.00	-2.36	-2.55 ± 0.20	-2.17 ± 0.20	-310	4	
Pristine_252.6959+09.4020	16:50:47.01	09:24:07.0	4761	1.69 ± 0.19	2.00	-2.33	-2.62 ± 0.21	-2.15 ± 0.20	-106	4	
Pristine_253.5853+16.2970	16:54:20.46	16:17:49.1	4582	1.02 ± 0.23	2.00	-3.00	-3.02 ± 0.21	-2.57 ± 0.20	+175	4	
Pristine_254.4746+11.3806	16:57:53.90	11:22:50.0	4818	1.85 ± 0.08	2.00	-2.61	-3.08 ± 0.17	-2.58 ± 0.20	-230	5	
Pristine_254.5655+13.1590	16:58:15.71	13:09:32.4	5105	3.07 ± 0.24	1.50	-2.57	-2.78 ± 0.34	-2.61 ± 0.20	-162	5	
Pristine_254.7635+17.2190	16:59:03.22	17:13:08.4	5297	2.89 ± 0.30	1.80	-2.57	-3.43 ± 0.42	-2.94 ± 0.20	-149	6	
Pristine_254.8233+12.6074	16:59:17.57	12:36:26.6	5793	3.59 ± 0.04	1.50	-2.59	-3.12 ± 0.20	-2.84 ± 0.20	+13	6	
Pristine_134.5085+15.3492	08:58:02.02	15:20:57.3	6493	4.52 ± 1.00	1.50		-2.21 ± 0.40	-1.71 ± 0.30	-21	6	
Pristine_134.8974+18.1561 <sup>a</sup>	08:59:35.40	18:09:22.1	5624	2.77 ± 1.45	1.80	-2.40	-3.37 ± 0.20	-2.87 ± 0.30	-73	6	
Pristine_185.3534+06.6021	12:21:24.81	06:36:07.8	6641	4.15 ± 0.35	1.50	-1.70	-1.54 ± 0.40	-1.31 ± 0.20	+47	6	
Pristine_189.9859+09.1684	12:39:56.61	09:10:06.5	6593	4.38 ± 0.17	1.50	-0.80	-2.00 ± 0.30	-1.59 ± 0.20	+80	5	
Pristine_193.4392+06.2295	12:53:45.41	06:13:46.2	6320	4.14 ± 0.38	1.50	-1.54	-2.32 ± 0.20	-1.89 ± 0.20	-43	6	
Pristine_218.7940+09.2376	14:35:10.55	09:14:15.4	5742	3.45 ± 0.27	1.50	-2.46	-2.33 ± 0.25	-2.18 ± 0.30	+313	6	
Pristine_220.7009+13.1405	14:42:48.20	13:08:25.6	5639	1.44 ± 2.00	2.00	-1.89	-3.08 ± 0.20	-2.71 ± 0.30	-68	7	
Pristine_225.4126+06.9134	15:01:39.05	06:54:48.3	6845	4.52 ± 0.26	1.50	-1.12	-1.86 ± 0.30	-1.66 ± 0.30	-19	6	
Pristine_228.1376+12.2612	15:12:33.02	12:15:40.2	5447	3.29 ± 0.48	1.50	-2.03	-3.00 ± 0.40	-2.72 ± 0.30	-136	5	
Pristine_233.5160+15.9466	15:34:03.86	15:56:48.1	6616	3.89 ± 0.55	1.50	-1.33	-2.28 ± 0.20	-1.77 ± 0.20	-51	6	
Pristine_238.7984+13.4432	15:55:11.61	13:26:35.7	5245	2.77 ± 0.85	1.80	-1.87	-3.02 ± 0.40	-2.61 ± 0.30	-60	5	
Pristine_239.0673+04.4411	15:56:16.20	04:26:27.7	5815	4.65 ± 0.09	1.00	-1.97	-3.80 ± 0.40	-3.33 ± 0.30	-73	6	
Pristine_240.8121+07.2526	16:03:14.90	07:15:09.5	6485	4.03 ± 0.25	1.50	-1.35	-1.50 ± 0.20	-1.40 ± 0.30	+0	5	
Pristine_242.4202+17.8114	16:09:40.84	17:48:41.0	5929	3.08 ± 0.64	1.50	-1.32	-2.00 ± 0.40	-1.97 ± 0.40	+117	5	
Pristine_246.4552+14.2016	16:25:49.26	14:12:05.9	6471	4.20 ± 0.19	1.50	-1.22	-2.38 ± 0.40	-2.09 ± 0.30	-20	8	
Pristine_247.2527+05.6626	16:29:00.64	05:39:45.4	5661	3.18 ± 0.61	1.50	-1.72	-2.77 ± 0.40	-2.20 ± 0.50	+54	6	
Pristine_247.9296+17.6603	16:31:43.10	17:39:37.0	5127	2.08 ± 0.17	1.80	-2.64	-2.87 ± 0.30	-2.49 ± 0.30	+41	3	
Pristine_250.2948+14.9801	16:41:10.76	14:58:48.5	6638	3.89 ± 0.31	1.50	-1.18	-2.67 ± 0.30	-2.37 ± 0.30	-45	8	
Pristine_253.2195+11.3874	16:52:52.70	11:23:14.6	6434	3.92 ± 0.32	1.50	-1.53	-3.00 ± 0.30	-2.58 ± 0.30	-81	5	
Pristine_255.8743+11.3281	17:03:29.83	11:19:41.3	5385	2.66 ± 0.88	1.80	-2.09	-2.60 ± 0.30	-2.41 ± 0.30	+72	6	
Pristine_140.1321+16.4130 <sup>a</sup>	09:20:31.71	16:24:46.7	6404	3.14 ± 0.70	1.50	-2.34		-1.70 ± 0.30	+133	6	
Pristine_140.6414+16.7636 <sup>a</sup>	09:22:33.93	16:45:49.2	6388	4.34 ± 0.24	1.50	-3.33		-1.90 ± 0.30	+77	5	
Pristine_149.7205+15.3115	09:58:52.91	15:18:42.0	6377	4.81 ± 0.18	1.50	-2.44		-2.64 ± 0.30	-57	6	
Pristine_151.6456+15.9545	10:06:34.93	15:57:16.2	5058	2.91 ± 1.00	1.80	-3.26		-2.84 ± 0.40	+82	5	
Pristine_183.0629+00.4536	12:12:15.08	00:27:13.3	6548	4.68 ± 0.17	1.50	-1.45		-1.78 ± 0.30	-7	6	
Pristine_184.2955+02.2702	12:17:10.92	02:16:12.6	5713	2.27 ± 1.00	1.80	-1.87		-2.51 ± 0.30	+139	10	
Pristine_202.9418+11.5464	13:31:46.03	11:32:47.2	6310	3.40 ± 0.71	1.50	-1.23		-2.47 ± 0.30	+45	6	
Pristine_205.9426+13.4095	13:43:46.23	13:24:34.4	5506	2.86 ± 0.82	1.80	-1.59		-2.60 ± 0.40	+83	5	
Pristine_208.0555+08.8014	13:52:13.32	08:48:05.0	5444	1.67 ± 2.00	2.00	-2.09		-2.66 ± 0.20	+143	5	
Pristine_243.8528+06.6345	16:15:24.67	06:38:04.0	4886	1.70 ± 1.20	2.00	-3.19		-0.65 ± 0.40	-5	2	
Pristine_181.9215+09.7465	12:07:41.17	09:44:47.4	6286	1.42 ± 1.70	2.00	-0.87					

Star	RA J2000	Dec J2000	$T_{\text{eff}}$ K	$\log g$ cgs	$\xi$ kms <sup>-1</sup>	[Fe/H] <sub>phot</sub> dex	[Fe/H] dex	[Ca/H] <sub>CaK</sub> dex	$V_{\text{rad}}$	$\delta V_{st}$ kms <sup>-1</sup>	$\delta$
Pristine_231.3300+03.2701	15:25:19.20	03:16:12.5	4757	3.66 ± 1.00	1.50						
Pristine_133.9563+15.8948	08:55:49.52	15:53:41.4	5815	2.29 ± 1.00	1.80	-2.80					
Pristine_186.9046+12.4967	12:27:37.11	12:29:48.5	6504	4.06 ± 0.35	1.50	-2.63					
Pristine_241.0593+07.7943	16:04:14.27	07:47:39.1	6719	4.36 ± 0.16	1.50	-1.08					
Pristine_250.0644+17.2451	16:40:15.47	17:14:42.2	6312	3.70 ± 0.37	1.50	-0.53					
Pristine_250.4673+15.1604	16:41:52.14	15:09:37.5	6569	4.21 ± 0.16	1.50	-1.63					

<sup>a</sup> weak H-line EWs.

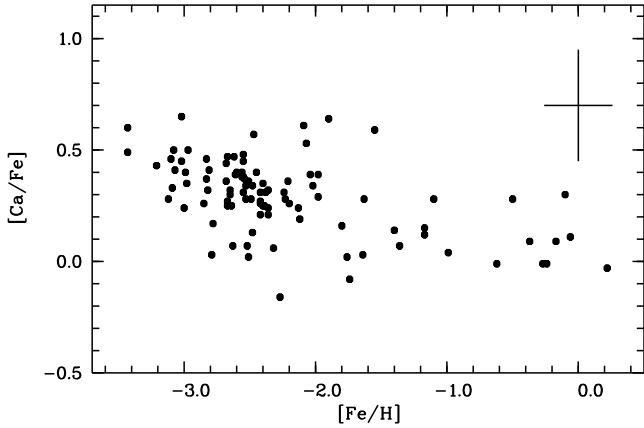


**Figure 4.**  $[Ca/Fe]$  derived from the Ca II-K line vs.  $[Fe/H]$ . A typical uncertainty is shown for the Fe and Ca abundances (horizontal and vertical segment, respectively).

For the more metal-rich stars and the best-quality spectra (98 stars), we were able to derive the abundance for several elements, while for the poor-quality and/or more metal-poor stars, we derived only a metallicity estimate. For 128 spectra we derived the Ca abundance by fitting the Ca II-K line, with six uncertain cases (Pristine\_242.4202+17.8114, Pristine\_246.4552+14.2016, Pristine\_247.2527+05.6626, Pristine\_250.2948+14.9801, Pristine\_205.9426+13.4095 and Pristine\_243.8528+06.6345). The Ca II-K line is strong and formed close to local thermodynamical equilibrium (LTE). At low resolution, it can be contaminated by inter-stellar absorption (see e.g. Caffau et al. 2012).

For the 98 stars for which we could derive detailed chemical composition, we have a large spread in metallicity, in the range  $-3.43 < [Fe/H] < +0.22$  with a standard deviation of 0.81. In period 103 we have detailed chemical investigation for 72 stars and we derived  $\langle [Fe/H] \rangle = -2.43 \pm 0.67$ . The 11 stars, within the 98 with detailed chemical investigation, with  $[Fe/H] \leq -3.0$  are all observations of period 103.

For 127 stars we derived the Ca abundance from the Ca II-K line and for 90 stars  $A(Ca)$  from Ca I lines. In Figure 4, the Ca abundance derived from the Ca II-K line versus  $[Fe/H]$  is shown. On the upper-right corner of the figure, a typical uncertainty is shown: the horizontal segment represents the uncertainty on the Fe abundance, while the vertical one the uncertainty on the  $A(Ca)$  determination from the Ca II-K line. From the figure we can see that the most metal-rich stars have on average a  $[Ca/Fe]$  close to solar (for the 11 stars with  $[Fe/H] > -1$ ,  $\langle [Ca/Fe] \rangle = 0.09 \pm 0.12$ ), while in the metal-poor regime, most stars show the typical  $\alpha$ -enhancement. A few metal-poor stars show no  $\alpha$ -enhancement. As said above, the  $A(Ca)$  determination from the Ca II-K line could bring uncertainty due to contamination in this line, but at low-resolution in the metal-poor regime, this line is irreplaceable to derive the stellar metallicity. The line-to-line scatter for multiple-line abundances determinations, as well as the detailed abundances, are provided in the on-line table. A typical line-to-line scatter for  $\alpha$ -elements is of the order of 0.15 dex, for Fe I 0.25 dex. For the elements derived by a single line we expect a typical uncertainty of 0.3 dex.

In Figure 5, the Mg abundance is compared to  $A(Ca)$

from the Ca II-K line. The agreement is not perfect, but consistent with the low resolution of the spectra. In the lower panel of the figure,  $[Mg/Fe]$  vs.  $[Fe/H]$  is shown and in the upper-right corner of the plot, a representative uncertainty on the Fe (horizontal) and Mg (vertical) abundance determination is shown. Although the majority of the stars behave as expected ( $\alpha$ -normal at metal-rich regime and  $\alpha$ -enhanced at the metal-poor end), some metal-poor stars appear  $\alpha$ -normal or even  $\alpha$ -poor. This is not just due to uncertainties, also if they certainly play a role. For all the stars with detailed chemical analysis we could derive  $A(Mg)$ . The nine metal-poor stars with  $[Mg/Fe] < 0.0$  are in the metallicity range:  $-2.82 \leq [Fe/H] \leq -1.17$ . Their line-to-line scatter in Mg is very diverse, from large values up to 0.80 dex to very small quantities smaller than 0.15 dex for three stars. We are not surprised of the large line-to-line scatter for Mg due to the fact that the abundance is based on saturated lines in low-resolution spectra. Of this small sample of nine stars, two have  $[Ca/Fe] < 0$ , when Ca is derived from Ca I lines. Seven metal-poor stars in the sample have at the same time the three  $\alpha$  indicators (abundance from Mg I, Ca I and Ca II-K lines) giving  $[a/Fe] < 0.2$ ; three metal-poor stars have at the same time  $[Mg/Fe] < 0.1$  and  $[Ca/Fe] < 0.1$ . We are confident that the low- $\alpha$  stars are not just due to the low-resolution; in fact, similar observations with the same instrument and setting, analysed in the same way, produced a sample of 65 metal-poor stars all  $\alpha$ -enhanced (see Caffau et al. in preparation) as expected for stars in the low-metallicity regime. A high-resolution follow-up for some of these  $\alpha$ -normal, metal-poor stars would be desirable, to confirm or refute the results from our low resolution spectra.

We could investigate C, Ca, Ti, Cr, Fe, Ni, Sr and Ba, according to the quality of the spectra and the abundances of the stars. For few stars we could derive the abundance of three elements (Ca, Ti and Fe) from neutral and singly ionised elements. The comparison, presented in Figure 6, shows a general good agreement, confirming also the adopted surface gravity. For the most metal-poor stars with a complete chemical investigation (first part of Table 3), the only Ca I line we could detect, at 422.6 nm, leads to an underestimation of  $A(Ca)$  in LTE but also taking into account the departure from local thermodynamical equilibrium (NLTE, see Mashonkina et al. 2017; Spite et al. 2012) and for this reason in the Figure there is a hint of plateau at  $A(CaK)$  of about 3.6 for  $A(CaI) < 4$ . The fact that the  $A(Ti)$  abundance derived from Ti II lines is systematically larger than when derived from Ti I lines can be explained by NLTE effects (see Figures 1 and 6 by Mashonkina et al. 2016). The small NLTE effects on Fe I lines (Mashonkina et al. 2016) explain the good agreement between the  $A(Fe)$  derived from Fe I and Fe II lines.

Abundances or upper-limits on carbon could be derived for all the 98 stars for which we have a detailed chemical investigation, and also four  $A(C)$  measurements and 12 upper-limits could be derived for stars with only a metallicity determination. Two stars (Pristine\_229.5434+10.6323 with  $[Fe/H] = -1.64$  and Pristine\_248.3014+09.7034 with  $[Fe/H] = -2.07$ ) are carbon enhanced metal-poor (CEMP) stars, both belonging to the high C-band as defined by Spite et al. (2013). Star Pristine\_229.5434+10.6323 is also highly enhanced in Ba.

For a very few stars we could also derive the N abun-

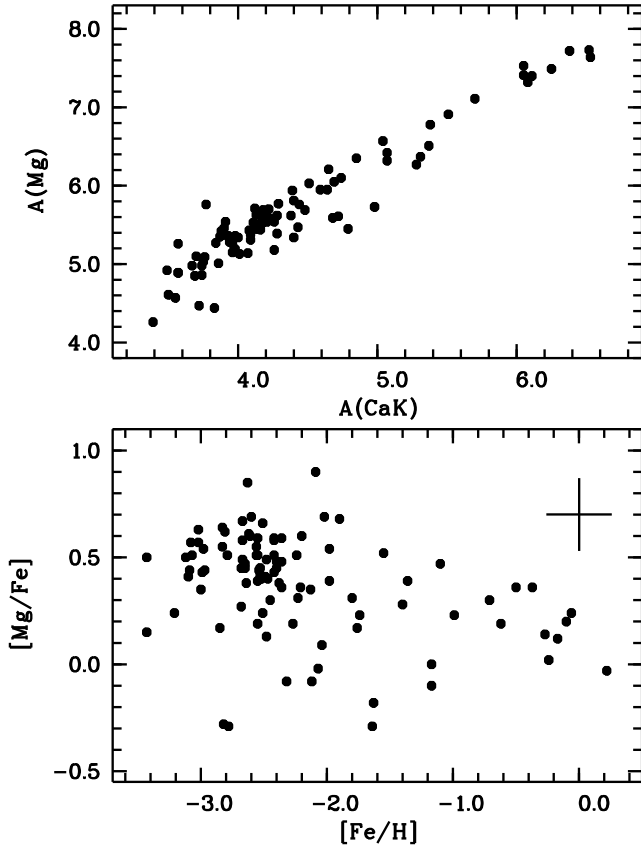


**Figure 5.** Upper panel: Mg abundance versus  $A(\text{Ca})$  from the  $\text{Ca II-K}$  line. Lower panel:  $[\text{Mg}/\text{Fe}]$  vs.  $[\text{Fe}/\text{H}]$ . The horizontal and vertical bars represent a typical uncertainty in the Fe and Mg abundance determination.

dance. The majority of the measurements are uncertain, due to the low resolution, and we could derive it only for the cooler stars, which happen to be all in the metal-poor regime. In Fig. 7 we compare  $[\text{C}/\text{Fe}]$ ,  $[\text{N}/\text{Fe}]$  and also  $[(\text{C}+\text{N})/\text{Fe}]$  to the high quality spectra done by Spite et al. (2005). Clearly the star-to-star scatter in our sample is much larger, but we see a very similar pattern. From the figure it is clear that the large star-to-star scatter in  $[\text{N}/\text{H}]$  is much reduced when looking at  $[(\text{C}+\text{N})/\text{Fe}]$ . In fact some of the luminous stars went through the second dredge-up so that their C abundance is reduced while the N abundance is enhanced. In Fig. 8,  $[\text{C}/\text{Fe}]$  and  $[(\text{C}+\text{N})/\text{Fe}]$  are plotted as a function of surface gravity, as a proxy for luminosity. There is a trend for lower  $[\text{C}/\text{Fe}]$  for the more evolved stars, which disappears in the case of  $[(\text{C}+\text{N})/\text{Fe}]$ , as expected from the theory of stellar evolution.

For a small subsample of stars, we could derive the abundances of Cr and Ni (see Figure 9) and of Sr and Ba (see Figure 10).

## 4 DISCUSSION AND CONCLUSIONS

### 4.1 Kinematics

Looking at the kinematics of the stars with  $[\text{Fe}/\text{H}] \leq -2.5$ , we find that only three stars have a maximum excursion  $z_{\text{max}} < 4$  kpc from the Milky Way plane. These stars are

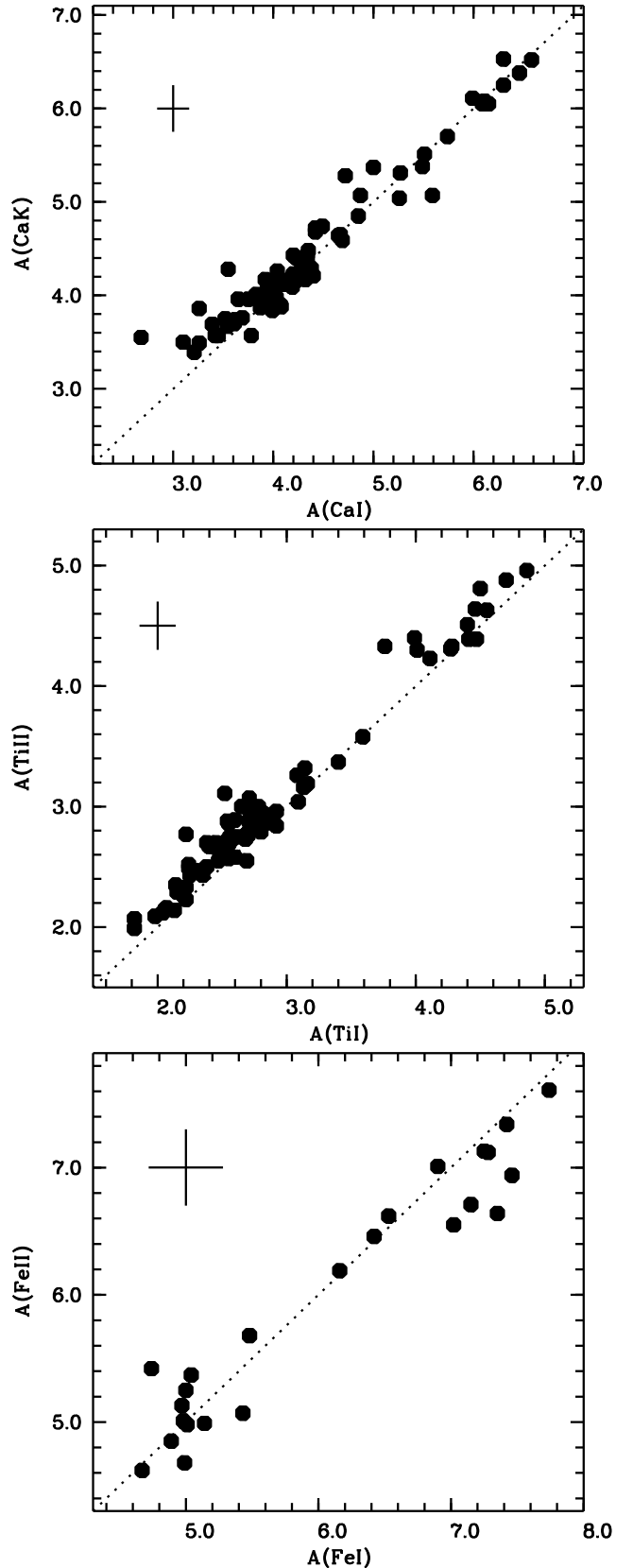


**Figure 6.** Comparison of the abundances derived from lines of neutral and single ionised element in the case of Ca, Ti and Fe. A typical uncertainty in shown in the upper-left corner of each panel.

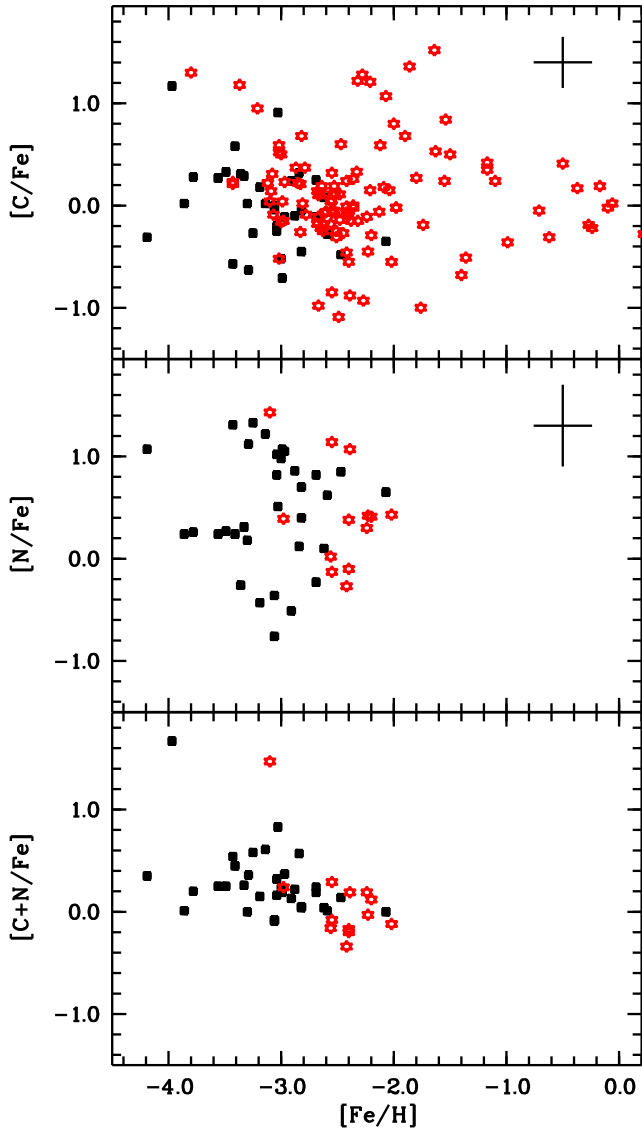


**Figure 7.** [C/Fe] (upper panel), [N/Fe] (central panel) and [C+N/Fe] (lower panel) as a function of [Fe/H] of our sample of stars (red stellar symbols) compared to the sample of Spite et al. (2005).

Pristine\_254.8233 + 12.6074, Pristine\_253.2195 + 11.3874, and Pristine\_239.0673 + 04.4411. Pristine\_239.0673 + 04.4411 is the most metal-poor star in the sample ([Fe/H] =  $-3.8$  with [Ca/Fe] = 0.47) and also the star that remains closer to the Milky Way plane,  $z_{\max} = 1.46^{+0.81}_{-0.58}$ ; it is moving with a prograde motion with an intermediate eccentricity,  $\epsilon = 0.53^{+0.09}_{-0.11}$ . The other two stars, Pristine\_254.8233 + 12.6074 and Pristine\_253.2195 + 11.3874, have a metallicity in the EMP regime, and have respectively a retrograde and a prograde orbit. Pristine\_254.8233 + 12.6074 is the most  $\alpha$ -poor among these three stars. As demonstrated by the simulations of Jean-Baptiste et al. (2017), the fact that a star belongs to a given kinematic group does not allow by itself to decide if the star has been accreted or has been formed *in situ*. A major merger occurring after the thick disc is formed, heats the thick disc and some thick disc stars can end up in retrograde orbits. Stars from the merging galaxy, can occupy the

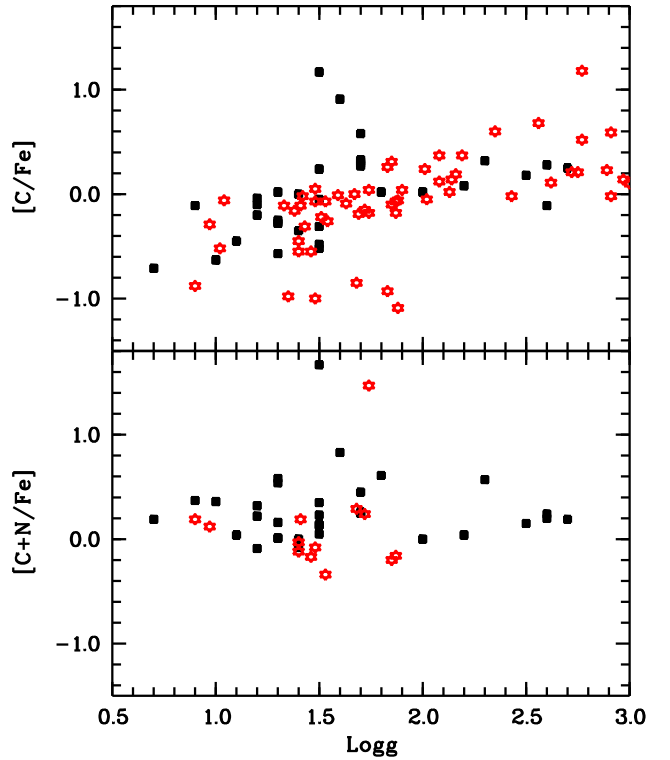


**Figure 8.** [C/Fe] (upper panel) and [C+N/Fe] (lower panel) vs. the surface gravity of our sample of stars (red stellar symbols) compared to the sample of Spite et al. (2005).

same kinematic group. It is thus impossible to speculate on the origin of these retrograde stars. Yet we may confidently assign the two above stars on prograde orbits to the thick disc.

We thus find only two stars, out of 55, with [Fe/H]  $\leq -2.5$ , Pristine\_253.2195 + 11.3874 and Pristine\_239.0673 + 04.4411, that belong to the thick disc. This fraction is lower than the percentage found by Sestito et al. (2019a); Di Matteo et al. (2019); Sestito et al. (2019b). Were this sample similar in behaviour, we should have expected about 14 thick disc stars. The orbital parameters for the stars with [Fe/H]  $\leq -2.5$  are provided as on-line material.

#### 4.2 Abundances: $\alpha$ -elements

One interesting result of this study is that some metal-poor stars in our sample appear not to be enhanced in  $\alpha$ -elements. In Figure 11 the average of [Mg/Fe] and [Ca/Fe] is used as a proxy for  $\alpha$  and shown as a function of [Fe/H]. Some of the stars really appear poor in  $\alpha$  elements. These stars are, on average, both more  $\alpha$ -poor and metal-poor than the sample of Nissen, & Schuster (2010). The existence of  $\alpha$ -poor metal-poor stars is not a new result (Ivans et al. 2003; Cohen et al. 2013; Caffau et al. 2013a; Susmitha Rani et al. 2016; Bonifacio et al. 2018; François et al. 2018), but their number is steadily increasing. In Figure 12, [Mg/Fe] as a function of [Fe/H] for our sample of stars is compared to two reference samples: the Mg abundance derived by Andrievsky et al. (2010) in the sample from First Stars ESO Large Programme (Cayrel et al. 2004) and to the sample from Nissen, & Schuster (2010). Our sample is, on average,



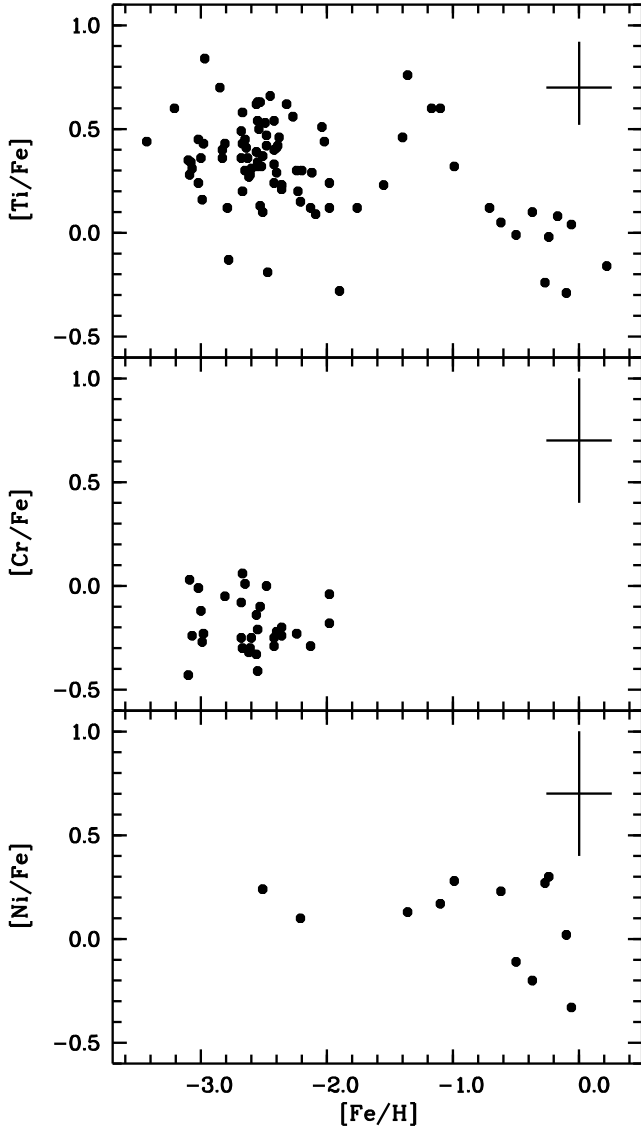


Figure 9. Abundances of Ti, Cr, Mn and Ni versus  $[\text{Fe}/\text{H}]$ .

more metal-rich than the sample by [Andrievsky et al. \(2010\)](#) and more metal-poor than the sample of [Nissen, & Schuster \(2010\)](#). There is anyway a general agreement for the metal-poor,  $\alpha$ -normal population. [Haywood et al. \(2018\)](#), in the light of the Gaia DR2 data, have argued that the low- $\alpha$  stars in the [Nissen, & Schuster \(2010\)](#) sample were formed in a massive satellite galaxy, that underwent a major merger with the Milky Way (see also [Belokurov et al. 2018](#); [Helmi et al. 2018](#)). The high- $\alpha$  sequence, instead, corresponds to the thick disk. Both for the [Nissen, & Schuster \(2010\)](#) and from other data in the literature it is clear that the two sequences merge at low metallicity and the two populations become equally  $\alpha$  enhanced (also see the recent dynamical analysis of metal-poor dwarfs in the outer halo by [Monty et al. 2019](#)). The low- $\alpha$  stars in the present sample seem to belong to a different population with respect to the [Nissen, & Schuster \(2010\)](#) low- $\alpha$  stars, except, perhaps, for [Pristine\\_233.5763+03.4486](#) and [Pristine\\_245.9038+05.939](#), that, within errors, are compatible with the [Nissen, & Schuster \(2010\)](#) low- $\alpha$  sequence. Unfor-

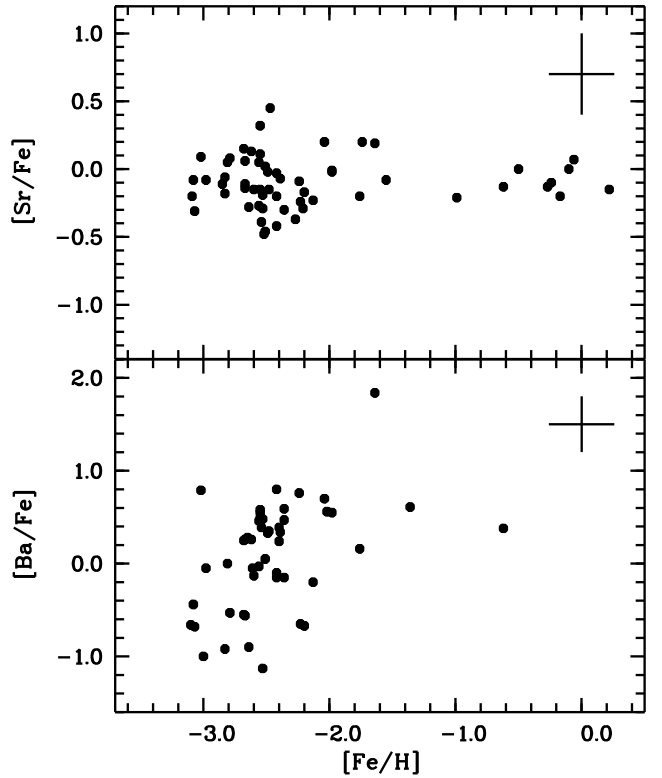


Figure 10. Abundances of Sr and Ba versus  $[\text{Fe}/\text{H}]$ .

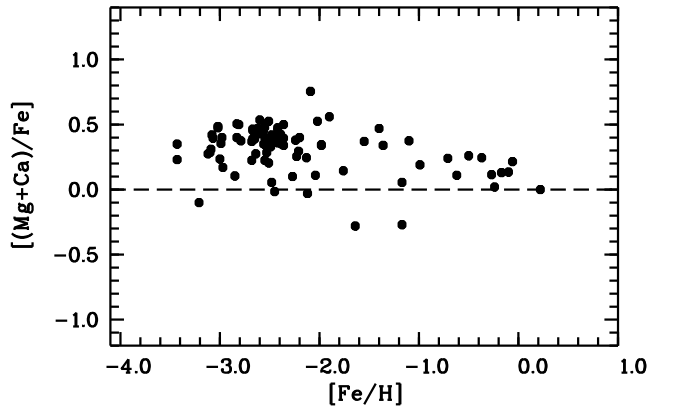
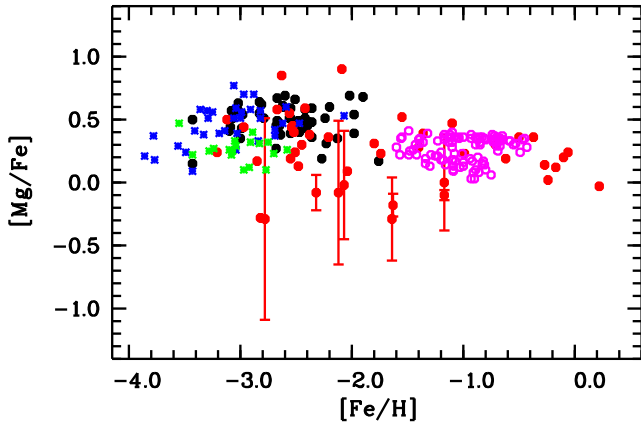


Figure 11.  $[\alpha/\text{Fe}]$  versus  $[\text{Fe}/\text{H}]$  for the 98 stars with detailed chemical investigation.

tunately, we obtain large uncertainties on the orbital parameters for the most  $\alpha$ -poor ( $[\text{Ca}/\text{Fe}] \leq 0.1$ ) stars, except for [Pristine\\_250.2762 + 09.2517](#) (the Ca abundance is from the Ca II-K line), where we can classify it as an inner halo star in prograde motion.

At the other end of the Mg abundances [Pristine\\_249.1867+05.9980](#) is extremely enhanced in Mg and also in Ca. Not as Mg enhanced as [CS 22949-037](#) ([Depagne et al. 2002](#); [Norris et al. 2002](#)) or [SDSS J1349+1407](#) ([Bonifacio et al. 2018](#)), nor is the  $[\text{Mg}/\text{Ca}]$  ratio as high. Also [Pristine\\_250.2762+09.2517](#) has a very high  $[\text{Mg}/\text{Ca}]$  ratio, however its  $[\text{Ca}/\text{Fe}]$  is close to zero according to the Ca II K line.



**Figure 12.**  $[\text{Mg}/\text{Fe}]$  versus  $[\text{Fe}/\text{H}]$ . Filled symbols are the stars here analysed, red unevolved ( $\log g \geq 3$ ) and black evolved ( $\log g < 3$ ) stars. For the metal-poor stars with  $[\text{Mg}/\text{Fe}] < 0$  we plot also the line-to-line scatter of Mg. Open pink circles are from [Nissen, & Schuster \(2010\)](#) (all these stars are unevolved); cross symbols are the LTE  $[\text{Mg}/\text{Fe}]$  from [Andrievsky et al. \(2010\)](#) (green unevolved and blue evolved stars).

#### 4.3 Abundances: Ca

In Figure 13, the comparison between the  $A(\text{Ca})$  derived from the  $\text{Ca II-K}$  line and the photometric metallicity is shown. Due to the difference in the selection strategy, filled symbols represent stars observed in ESO period 103, while open stellar symbols represent observations of ESO periods 100 and 101. We also divided the stars in evolved ( $\log g < 3.0$ ) and un-evolved ( $\log g \geq 3.0$ ) stars. This is a rough division, just to highlight (as already mentioned by [Bonifacio et al. 2019](#)) that the metallicity estimate here used is very efficient for giants, but it is not effective for dwarf stars. The photometric abundances used to select the stars observed in ESO period 103, thus taking advantage of the Gaia parallaxes, agree better with the spectroscopic metallicities.

#### 4.4 Abundances: heavy-elements

We compared our stars with measurable Sr and Ba for stars with  $[\text{Fe}/\text{H}] \leq -1.6$  with the literature and we could find a similar behaviour (see Figure 14) for  $[\text{Sr}/\text{Ba}]$  versus  $[\text{Ba}/\text{Fe}]$ . The star in the lower right side of the plot (Pristine\_229.5434+10.6323) is in fact a CEMP star. Few stars of our sample appear in the underpopulated space on the lower right panel; they could be interesting and higher resolution follow-up would be desirable. This clear upward trend of  $[\text{Sr}/\text{Ba}]$  with decreasing  $[\text{Ba}/\text{Fe}]$  well visible in the figure was investigated for high-resolution observations (see e.g. [Spite et al. 2005, 2014](#)) and recently also for low-resolution observations ([Caffau et al. 2018](#)). This finding confirms once more the earlier conclusions by [Mashonkina et al. \(2017\)](#), who stated that  $[\text{Sr}/\text{Ba}]$  of the VMP stars in the Milky Way and classical dSphs reveal two branches in the  $[\text{Sr}/\text{Ba}]$  versus  $[\text{Ba}/\text{H}]$  plane, but not simply a scatter of data.

#### 4.5 Success rate

In this work, we analysed a sample of stars selected with photometry, by using the narrow-band *CaHK* Pristine photom-

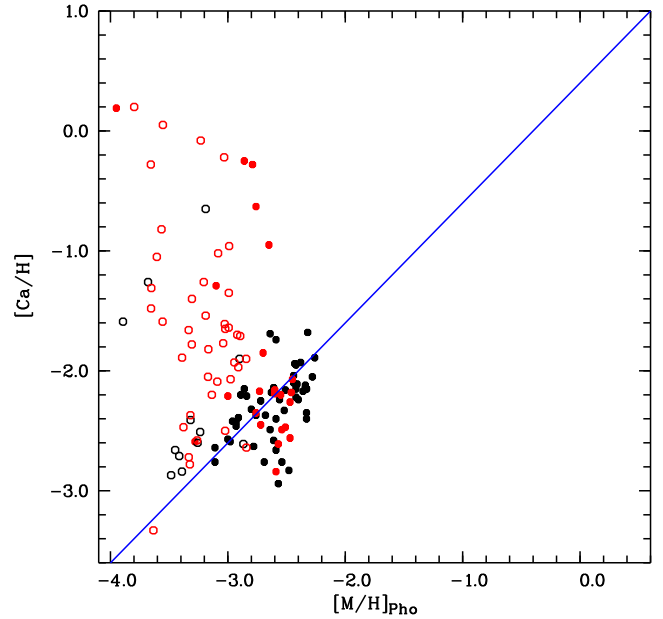


**Figure 13.**  $[\text{Ca}/\text{H}]$  derived from the  $\text{Ca II-K}$  line vs. the photometric metallicity used for target selection. Filled symbols are stars observed in ESO period 103, open symbols are stars observed in ESO periods 100 and 101. Red symbols refer to unevolved star ( $\log g \geq 3$ ) and black to evolved stars ( $\log g < 3$ ). The solid line shows the correspondence of the two, assuming a Ca-enhancement of 0.4 for all stars.

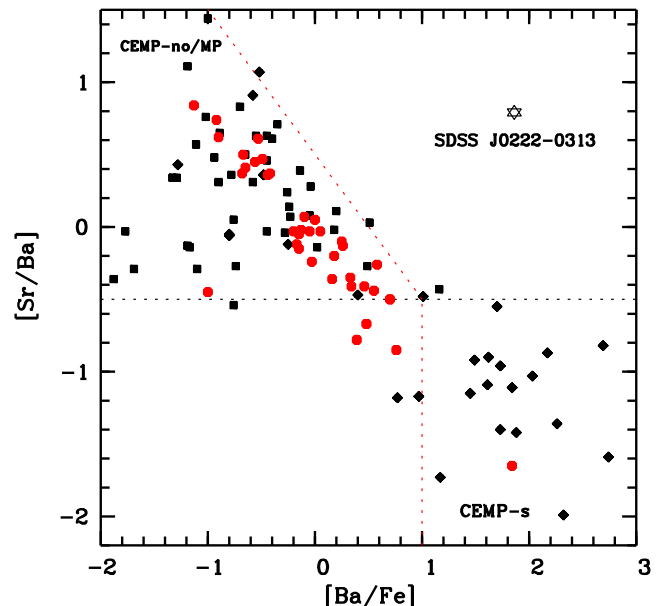


**Figure 14.**  $[\text{Sr}/\text{Ba}]$  as a function of  $[\text{Ba}/\text{Fe}]$ : red circles are stars here analysed; black squares are from [Spite et al. \(2005\)](#), the black diamonds are CEMP stars from the literature ([Aoki et al. 2001; Barbuy et al. 2005; Sivarani et al. 2006; Behara et al. 2010; Spite et al. 2013; Yong et al. 2013](#)). The black star is the CEMP star SDSS J0222-0313 ([Caffau et al. 2019](#)). The black horizontal dashed line is the r-only solar value for  $[\text{Sr}/\text{Ba}]$  according to [Mashonkina, & Gehren \(2001\)](#). Normal stars are in the upper-left part of the diagram, sharing the surface with CEMP-no stars; CEMP-s stars are in the lower-right part of the diagram.

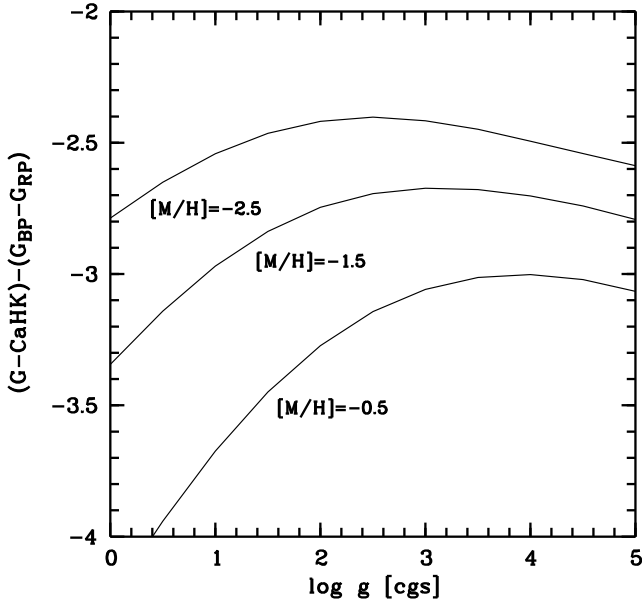


**Figure 15.** Theoretical colours, used in our calibration, as a function of  $\log g$  for  $T_{\text{eff}} = 5000$  K and for three different metallicities.

etry associated with the wide-band Gaia photometry and Gaia parallaxes. During the first two observing periods the Gaia parallaxes were not available and we had to rely only on colours for the selection. Nevertheless the efficiency of selection of metal-poor stars is very high. Of the 54 stars observed in ESO periods 100 and 101, 17 have a metallicity that is below  $-2.5$ , i.e. a success rate of 31%. This success rate is lower than what reported in [Aguado et al. \(2019a\)](#), however this sample, as can be appreciated in Fig. 13, was selected to be heavily biased towards the stars with photometric metallicity estimate below  $-3.5$ , where the calibration is more uncertain and we have a higher rate of contamination. On the other hand for the stars observed in ESO period 103, 56 out of 74, i.e. 76% have a metallicity below  $-2.5$ . This shows the importance of relying on parallaxes, that allow to break the degeneracy of the dependence of the *CaHK* magnitude on surface gravity and metallicity. This fraction boosts to 81% if we restrict the sample to the stars with  $\log g \leq 3.0$ . The reason for this difference is illustrated in Fig. 15 where we show the run of the *CaHK* colour as a function of  $\log g$  for  $T_{\text{eff}} = 5000$  K and three different metallicities and one can appreciate that the lines get closer together at higher gravities. These numbers, particularly for the stars with  $\log g \leq 3.0$ , are very similar to the success rate of the SkyMapper EMP survey (see [Da Costa et al. 2019a](#)).

The drawback of using parallaxes is that one is limited to the volume where good parallaxes are available. Thus the calibration using parallaxes and the ones that use only colours are complementary. Unsurprisingly, for the stars selected in ESO periods 100 and 101, some of which have poor parallaxes, the calibration that uses Gaia colours and parallaxes performs much more poorly than on stars observed in ESO period 103, that have been selected to have parallaxes with relative error less than 33%.

We computed the absolute value of the difference between the Fe abundance and the photometric metallicity, derived from our calibration  $\Delta_{\text{Fe}} = |([\text{Fe}/\text{H}] - \text{Met}_{\text{PV}})|$ .

It is theoretically expected that at lower gravity the *CaHK* colour is more sensitive to metallicity, as can readily be inferred from Fig. 15. This is further enhanced by the fact that the lower gravity stars are also cooler, as can be appreciated from figure 11 of [Bonifacio et al. \(2019\)](#), that shows how the PristineV calibration is more sensitive for cooler stars. To confirm this theoretical prediction of better performance of the PristineV calibration for giant stars, we divided the  $\log g$  range 0.9–4.9 in four bins of 1 dex and resulting that the  $\Delta_{\text{Fe}}$  was increasing from lower to higher  $\log g$  values:

- $\log g$  0.9–1.9:  $\Delta_{\text{Fe}} = 0.22 \pm 0.24$  (36 stars);
- $\log g$  1.9–2.9:  $\Delta_{\text{Fe}} = 0.49 \pm 0.33$  (18 stars);
- $\log g$  2.9–3.9:  $\Delta_{\text{Fe}} = 0.67 \pm 0.61$  (34 stars);
- $\log g$  3.9–4.9:  $\Delta_{\text{Fe}} = 0.88 \pm 0.90$  (27 stars).

While the stars observed in ESO period 103 have all accurate parallaxes, this is not the case for the stars observed in the other two periods. Of the 54 stars, four have negative parallaxes, 24 have a relative error on parallax  $\Delta\varpi/\varpi \geq 0.33$  and 24 have a relative error on parallax less than 0.33. However, the stars with good parallaxes observed in ESO periods 100 and 101 are all dwarfs or TO stars, thus in the  $T_{\text{eff}}$ ,  $\log g$  range where the PristineV calibration performs worst. It is thus not surprising that the overall performance of the PristineV calibration is better for the stars observed in ESO period 103. To quantify the performance of the PristineV calibration we use the Ca abundance derived from the Ca II-K line that is available for 127 out of 128 stars for which abundances have been derived. For the comparison we subtract 0.4 dex to the Ca abundance to take into account the general  $\alpha$ -enhancement in metal poor stars.  $\Delta_{\text{Ca}} = ([\text{Ca}/\text{H}] - 0.4 - \text{Met}_{\text{PV}})$ . Clearly this latter is misleading in the metal-rich regime, but the focus here is on the metal-poor stars. In period 103 we observed 52 stars with  $\log g \leq 3.0$  and for these stars  $\langle \Delta_{\text{Ca}} \rangle = -0.09$  with a standard deviation of 0.27 dex. For the 22 stars with  $\log g > 3.0$  instead we have  $\langle \Delta_{\text{Ca}} \rangle = +0.5$  with a standard deviation of 1 dex. In the other two periods we observed 12 stars with  $\log g \leq 3.0$  and  $\langle \Delta_{\text{Ca}} \rangle = -0.5$  with a standard deviation of 0.9 dex. Of the 42 stars with  $\log g > 3.0$  analysed in ESO periods 100 and 101 only 40 have both a metallicity from the PristineV calibration and a Ca abundance from the Ca II-K line, for these stars we find  $\langle \Delta_{\text{Ca}} \rangle = -0.8$  and a standard deviation of 0.5 dex. If we further restrict to the 26 stars that have a relative error on parallax better than 0.33 we find  $\langle \Delta_{\text{Ca}} \rangle = -0.7$  and again a standard deviation of 0.5 dex.

The above analysis shows that the PristineV calibration provides metallicities that are accurate to 0.3 dex, with hardly any significant offset, for giant stars that have an accurate parallax. On the other hand for TO and dwarf stars the calibration has a poor performance, whatever the accuracy of the parallax.

#### 4.6 C-enhanced stars

Among the stars with a full chemical analysis we found two (Pristine.229.5434+10.6323,  $[\text{Fe}/\text{H}] = -1.64$  and Pristine.248.3014+09.7034,  $[\text{Fe}/\text{H}] = -2.07$ ) that are CEMP stars (according to the criterion  $[\text{C}/\text{Fe}] \geq 1$ ), one of which (Pristine.229.5434+10.6323) is also Ba-rich. Among the stars that have only the metallicity from the Ca II-K line we

found seven further stars (Pristine\_134.5085+15.3492, Pristine\_134.8974+18.1561, Pristine\_193.4392+06.2295, Pristine\_220.7009+13.1405, Pristine\_225.4126+06.9134, Pristine\_233.5160+15.9466, Pristine\_239.0673+04.4411) with  $[C/Fe] \geq 1.0$ , therefore a total of 9 CEMP stars. Six of these belong to the “low-carbon band”, according to the definition of Bonifacio et al. (2018), while the three remaining ones, Pristine\_229.5434+10.6323, Pristine\_220.7009+13.1405 and Pristine\_225.4126+06.9134, belong to the “high-carbon” band. Since the Pristine *CaHK* filter is largely free from any contamination from features of any carbon-bearing molecules our selection is totally unbiased with respect to C abundance (see Starkenburg et al. 2017a). In principle one may thus use our sample to estimate the frequency of CEMP stars. We have 90 stars with  $[Fe/H] \leq -2.0$  of which 7 CEMP, and 55 stars with  $[Fe/H] \leq -2.5$ , of which 3 CEMP. This provides a frequency of 8% and 5% respectively. If we adopt the criterion  $[C/Fe] \geq 0.7$  to define the CEMP stars, to compare to the results of the much larger sample of Aguado et al. (2019a), we find three stars, out of 28 with  $-3 < [Fe/H] < -2$ , i.e. 11% and four, out of 13 with  $[Fe/H] < -3$ , i.e. 31% to be compared to 41% and 58% respectively found in Aguado et al. (2019a). By adopting the percentages of Aguado et al. (2019a), we should expect about 11 CEMP stars in the iron range  $-3 < [Fe/H] < -2$  and more than 7 in the range  $[Fe/H] < -3$ . Our frequencies of CEMP stars are also much lower than those provided by Placco et al. (2014), using the  $[C/Fe] \geq 1$  criterion, i.e. 24% for both  $[Fe/H] \leq -2.0$  and  $[Fe/H] \leq -2.5$ . We compare to the “uncorrected” numbers in table 1 of Placco et al. (2014) since we applied no correction to the measured C abundance in giants with  $\log g < 2.0$ . Even if we restrict ourselves to the “low-carbon” band sample, and compare to the numbers of Placco et al. (2014) that do not take into account CEMP-s and CEMP-r/s stars, that lie on the the “high-carbon” band, our frequencies are definitely lower. We find 7% for stars with  $[Fe/H] \leq -2.0$ , to be compared to 10% in Placco et al. (2014) and 4% for stars with  $[Fe/H] \leq -2.5$ , to be compared to 13% in Placco et al. (2014). By adopting the percentages of Placco et al. (2014), we should find nine CEMP stars for  $[Fe/H] \leq -2.0$  and seven for  $[Fe/H] \leq -2.5$ .

The low frequency of C-enhanced stars in our sample may be an indication that the Pristine filter has some sensitivity to the carbon abundance and that by selecting low metallicity stars we select against C-enhanced stars. Although the head of the CN  $B^2\Sigma^+ - X^2\Sigma^+ (0-0)$  band at 388.3nm is cut off by the filter, there are several CH lines that fall in the filter passband. This may be appreciated in figure 1 of Caffau et al. (2016) where a CH line as strong as the CaII K line can be clearly seen in the spectrum of SDSS J092912.32+023817.0 ( $[Fe/H] = -4.97$ ,  $[C/Fe] = +4.16$ ). While this could easily explain the discrepancy with Placco et al. (2014), the discrepancy with the frequencies of Aguado et al. (2019a) is more difficult to explain, since both samples have been selected using the Pristine photometry. We defer a more detailed investigation of the issue to a future paper of the series.

## ACKNOWLEDGEMENTS

Based on observations collected at the European Southern Observatory under ESO programmes 0100.D-0559, 0101.D-0227, and 0103.D-0128. We gratefully acknowledge support from the French National Research Agency (ANR) funded project “Pristine” (ANR-18-CE31-0017). EC and PB are thankful to ESO - Santiago for hosting them during the preparation of this manuscript. The authors thank the International Space Science Institute, Berne, Switzerland for providing financial support and meeting facilities to the international team “Pristine”. NFM and FS acknowledge funding from CNRS/INSU through the Programme National Galaxies et Cosmologie and through the CNRS grant PICS07708. ES gratefully acknowledges funding by the Emmy Noether program from the Deutsche Forschungsgemeinschaft (DFG) This work has made use of data from the European Space Agency (ESA) mission *Gaia* (<https://www.cosmos.esa.int/gaia>), processed by the *Gaia* Data Processing and Analysis Consortium (DPAC, <https://www.cosmos.esa.int/web/gaia/dpac/consortium>). Funding for the DPAC has been provided by national institutions, in particular the institutions participating in the *Gaia* Multilateral Agreement.

Based on observations obtained with MegaPrime/MegaCam, a joint project of CFHT and CEA/DAPNIA at the Canada-France-Hawaii Telescope (CFHT) is operated by the National Research Council (NRC) of Canada, the Institut National des Sciences de lâĂŽUnivers of the Centre National de la Recherche Scientifique of France, and the University of Hawaii.

## REFERENCES

- Aguado, D. S., Youakim, K., González Hernández, J. I., et al. 2019a, MNRAS, 490, 2241  
Aguado, D. S., Ahumada, R., Almeida, A., et al. 2019b, ApJS, 240, 23  
Andrievsky, S. M., Spite, M., Korotin, S. A., et al. 2010, A&A, 509, A88  
Anthony-Twarog, B. J., Sarajedini, A., Twarog, B. A., et al. 2000, AJ, 119, 2882  
Aoki, W., Ryan, S. G., Norris, J. E., et al. 2001, ApJ, 561, 346  
Appenzeller, I., Fricke, K., Fürtig, W., et al. 1998, The Messenger, 94, 1  
Antia, H. M., & Basu, S. 2011, Gong-soho 24: A New Era of Seismology of the Sun and Solar-like Stars, 012034  
Bailer-Jones, C. A. L., Rybizki, J., Foesneau, M., et al. 2018, AJ, 156, 58  
Barbuy, B., Spite, M., Spite, F., et al. 2005, A&A, 429, 1031  
Beers, T. C., Preston, G. W., & Shectman, S. A. 1992, AJ, 103, 1987  
Beers, T. C., Preston, G. W., & Shectman, S. A. 1985, AJ, 90, 2089  
Behara, N. T., Bonifacio, P., Ludwig, H.-G., et al. 2010, A&A, 513, A72  
Belokurov, V., Erkal, D., Evans, N. W., et al. 2018, MNRAS, 478, 611  
Bland-Hawthorn, J., & Gerhard, O. 2016, ARA&A, 54, 529  
Bovy, J. 2015, ApJS, 216, 29  
Bonifacio, P., Caffau, E., Spite, M., et al. 2018, A&A, 612, A65  
Bonifacio, P., Caffau, E., Sestito, F., et al. 2019, MNRAS, 487, 3797



- Bressan, A., Marigo, P., Girardi, L., et al. 2012, *MNRAS*, 427, 127
- Brook, C. B., Kawata, D., Scannapieco, E., et al. 2007, *ApJ*, 661, 10
- Caffau, E., Ludwig, H.-G., Bonifacio, P., et al. 2010, *A&A*, 514, A92
- Caffau, E., Bonifacio, P., François, P., et al. 2012, *A&A*, 542, A51
- Caffau, E., Bonifacio, P., François, P., et al. 2013a, *A&A*, 560, A15
- Caffau, E., Bonifacio, P., Sbordone, L., et al. 2013b, *A&A*, 560, A71
- Caffau, E., Bonifacio, P., Spite, M., et al. 2016, *A&A*, 595, L6
- Caffau, E., Gallagher, A. J., Bonifacio, P., et al. 2018, *A&A*, 614, A68
- Caffau, E., Monaco, L., Bonifacio, P., et al. 2019, *A&A*, 628, A46
- Cayrel, R., Depagne, E., Spite, M., et al. 2004, *A&A*, 416, 1117
- Christlieb, N., Schörck, T., Frebel, A., et al. 2008, *A&A*, 484, 721
- Cohen, J. G., Christlieb, N., Thompson, I., et al. 2013, *ApJ*, 778, 56
- Da Costa, G. S., Bessell, M. S., Mackey, A. D., et al. 2019, *MNRAS*, 489, 5900
- Depagne, E., Hill, V., Spite, M., et al. 2002, *A&A*, 390, 187
- Di Matteo, P., Spite, M., Haywood, M., et al. 2019, arXiv e-prints, arXiv:1910.13769
- El-Badry, K., Bland-Hawthorn, J., Wetzel, A., et al. 2018, *MNRAS*, 480, 652
- François, P., Caffau, E., Bonifacio, P., et al. 2018, *A&A*, 620, A187
- Freeman, K., & Bland-Hawthorn, J. 2002, *ARA&A*, 40, 487
- Gaia Collaboration, Brown, A. G. A., Vallenari, A., et al. 2018, *A&A*, 616, A1
- Gao, L., Theuns, T., Frenk, C. S., et al. 2010, *MNRAS*, 403, 1283
- Griffen, B. F., Dooley, G. A., Ji, A. P., et al. 2018, *MNRAS*, 474, 443
- Hanuschik, R. W. 2003, *A&A*, 407, 1157
- Haywood, M., Di Matteo, P., Lehnert, M. D., et al. 2018, *ApJ*, 863, 113
- Helmi, A., Babusiaux, C., Koppelman, H. H., et al. 2018, *Nature*, 563, 85
- Howes, L. M., Casey, A. R., Asplund, M., et al. 2015, *Nature*, 527, 484
- Ishiyama, T., Sudo, K., Yokoi, S., et al. 2016, *ApJ*, 826, 9
- Ivans, I. I., Sneden, C., James, C. R., et al. 2003, *ApJ*, 592, 906
- Jean-Baptiste, I., Di Matteo, P., Haywood, M., et al. 2017, *A&A*, 604, A106
- Karlssohn, T., Bromm, V., & Bland-Hawthorn, J. 2013, *Reviews of Modern Physics*, 85, 809
- Keller, S. C., Schmidt, B. P., Bessell, M. S., et al. 2007, *Publ. Astron. Soc. Australia*, 24, 1
- Keller, S. C., Bessell, M. S., Frebel, A., et al. 2014, *Nature*, 506, 463
- Koposov, S. E., Gilmore, G., Walker, M. G., et al. 2011, *ApJ*, 736, 146
- Kurucz, R. L. 2005, *Memorie della Societa Astronomica Italiana Supplementi*, 8, 14
- Lodders, K., Palme, H., & Gail, H.-P. 2009, *Landolt & Bornstein*, 4B, 712
- Mashonkina, L., & Gehren, T. 2001, *A&A*, 376, 232
- Mashonkina, L. I., Sitnova, T. N., & Pakhomov, Y. V. 2016, *Astronomy Letters*, 42, 606
- Mashonkina, L., Jablonka, P., Sitnova, T., et al. 2017, *A&A*, 608, A89
- Monty, S., Venn, K. A., Lane, J. M. M., et al. 2019, arXiv e-prints, arXiv:1909.11969
- Nissen, P. E., & Schuster, W. J. 2010, *A&A*, 511, L10
- Nordlander, T., Bessell, M. S., Da Costa, G. S., et al. 2019, *MNRAS*, 488, L109
- Norris, J. E., Ryan, S. G., Beers, T. C., et al. 2002, *ApJ*, 569, L107
- Pallottini, A., Gallerani, S., & Ferrara, A. 2014, *MNRAS*, 444, L105
- Placco, V. M., Frebel, A., Beers, T. C., et al. 2014, *ApJ*, 797, 21
- Salvadori, S., Ferrara, A., Schneider, R., et al. 2010, *MNRAS*, 401, L5
- Sbordone, L., Bonifacio, P., Castelli, F., & Kurucz, R. L. 2004, *Memorie della Societa Astronomica Italiana Supplementi*, 5, 93
- Sbordone, L., Caffau, E., Bonifacio, P., et al. 2014, *A&A*, 564, A109
- Schlafly, E. F., & Finkbeiner, D. P. 2011, *ApJ*, 737, 103
- Schönrich, R., Binney, J., & Dehnen, W. 2010, *MNRAS*, 403, 1829
- Sestito, F., Longeard, N., Martin, N. F., et al. 2019, *MNRAS*, 484, 2166
- Sestito, F., Martin, N. F., Starkenburg, E., et al. 2019, arXiv e-prints, arXiv:1911.08491
- Simon, J. D., Geha, M., Minor, Q. E., et al. 2011, *ApJ*, 733, 46
- Sivarani, T., Beers, T. C., Bonifacio, P., et al. 2006, *A&A*, 459, 125
- Spite, M., Cayrel, R., Plez, B., et al. 2005, *A&A*, 430, 655
- Spite, M., Andrievsky, S. M., Spite, F., et al. 2012, *A&A*, 541, A143
- Spite, M., Caffau, E., Bonifacio, P., et al. 2013, *A&A*, 552, A107
- Spite, M., Spite, F., Bonifacio, P., et al. 2014, *A&A*, 571, A40
- Starkenburg, E., Martin, N., Youakim, K., et al. 2017, *MNRAS*, 471, 2587
- Starkenburg, E., Oman, K. A., Navarro, J. F., et al. 2017, *MNRAS*, 465, 2212
- Starkenburg, E., Aguado, D. S., Bonifacio, P., et al. 2018, *MNRAS*, 481, 3838
- Susmitha Rani, A., Sivarani, T., Beers, T. C., et al. 2016, *MNRAS*, 458, 2648
- Tan, K., Chen, Y., Carrell, K., et al. 2014, *ApJ*, 794, 60
- Tumlinson, J. 2010, *ApJ*, 708, 1398
- Venn, K. A., Kieft, C. L., Sestito, F., et al. 2020, *MNRAS*, 492, 3241
- White, S. D. M., & Springel, V. 2000, *The First Stars*, 327
- Wolf, C., Onken, C. A., Luvaul, L. C., et al. 2018, *Publ. Astron. Soc. Australia*, 35, e010
- Yong, D., Norris, J. E., Bessell, M. S., et al. 2013, *ApJ*, 762, 26
- York, D. G., Adelman, J., Anderson, J. E., et al. 2000, *AJ*, 120, 1579
- Youakim, K., Starkenburg, E., Aguado, D. S., et al. 2017, *MNRAS*, 472, 2963

This paper has been typeset from a  $\text{\TeX}/\text{\LaTeX}$  file prepared by the author.